Available online at www.sciencedirect.com

SCIENCE DIRECT®

Journal of Catalysis 239 (2006) 376–389

JOURNAL OF CATALYSIS

www.elsevier.com/locate/jcat

Bifunctional nature of a SiO_2-supported Ni_2P catalyst for hydrotreating: EXAFS and FTIR studies

Yong-Kul Lee, S. Ted Oyama *

Environmental Catalysis and Nanomaterials Laboratory, Department of Chemical Engineering, (0211) Virginia Tech, Blacksburg, VA 24061, USA

Received 27 August 2005; revised 12 December 2005; accepted 16 December 2005

Abstract

A Ni_2P catalyst supported on a high-surface area SiO_2 (350 $m^2\ g^{-1}$) was prepared by temperature-programmed reduction, and its structural and surface properties were studied. X-ray diffraction and extended X-ray absorption fine structure measurements were used to obtain structural parameters for the supported Ni_2P phase, and Fourier transform infrared (FTIR) analysis with the probe molecules CO and pyridine was carried out to characterize the surface properties. The catalytic activity was measured at 573 K and 3.1 MPa in a three-phase fixed-bed reactor for hydrodesulfurization (HDS) and hydrodenitrogenation (HDN) using a model liquid feed. At standard conditions using 500 ppm S as 4,6-dimethyldibenzothiophene (4,6-DMDBT), 3000 ppm S as dimethyldisulfide, 200 ppm N as quinoline, and 1% tetralin in a tridecane solvent, the Ni_2P/SiO_2 gave an HDS conversion of 85%, an HDN conversion of 100%, and a tetralin conversion of 37%, which were much higher than those of a commercial Ni–Mo–S/Al_2O_3 catalyst, which gave an HDS conversion of 41%, an HDN conversion of 98%, and a tetralin conversion of 20% based on equal numbers of sites (240 µmol) loaded in the reactor. The sites were counted by CO chemisorption for the phosphide and by low-temperature O_2 chemisorption for the sulfide. The Ni_2P/SiO_2 catalyst favored the hydrogenation (HYD) pathway for 4,6-DMDBT HDS to generate methylcyclohexyltoluene and dimethylbicyclohexane with a relative HYD selectivity of 95%. It also favored hydrogenation for tetralin to give decalin with a relative HYD selectivity of 89%. The Ni_2P/SiO_2 catalyst also showed better resistance to N-compounds than the Ni–Mo–S/Al_2O_3 catalyst. The FTIR spectra of adsorbed CO showed that the Ni site in the Ni_2P phase gave rise to considerable π-back bonding, which was related to the high activity of the Ni_2P/SiO_2 catalyst in the hydrogenation of aromatics. The FTIR spectra of adsorbed pyridine showed that the Ni_2P phase had a P–OH group associated with Brønsted acidity that was active for the protonation of N compounds. These results thus suggest that the supported Ni_2P catalyst has bifunctional properties that are beneficial for catalytic activity in hydroprocessing.

Keywords: Nickel phosphide; XRD; EXAFS; 4,6-Dimethyldibenzothiophene; Hydrodesulfurization; Hydrodenitrogenation

---

1. Introduction

Considerable concerns for cleaner air and more stringent regulations of the sulfur content of transportation fuels and non-road fuels have put considerable pressure on the refining industry worldwide to produce cleaner fuels and have motivated much research for the development of new hydrotreating catalysts. The sulfur problem is becoming more serious in general because the allowed sulfur content, particularly of diesel fuels, is becoming much lower (<15 ppm by 2006), whereas the sulfur content of crude oils is becoming increasingly higher (average increase from 0.87% in 1981 to 1.42% in 2001) [3]. The challenge for deep desulfurization of diesel fuels is the difficulty in removing refractory sulfur compounds, such as 4,6-dimethyldibenzothiophene (4,6-DMDBT), by conventional hydrodesulfurization (HDS) processes. This problem is exacerbated by the presence of nitrogen compounds that adsorb competitively with the sulfur-containing species. New catalysts have thus been developed to enhance the activity for HDS of compounds like 4,6-DMDBT and to carry out simultaneous hydrodenitrogenation (HDN). Among alternatives to the widely used sulfides are transition-metal carbides, nitrides, and phosphides [4–9]. Metal phosphides are a novel catalyst group for deep hydrotreating and have received much attention due to their high activity for HDS and HDN of petroleum feed-

---

* Corresponding author.
E-mail address: oyama@vt.edu (S.T. Oyama).

0021-9517/$ – see front matter © 2006 Elsevier Inc. All rights reserved.
doi:10.1016/j.jcat.2005.12.029

stocks [9,15–17]. Transition-metal phosphide catalysts have been studied in hydrogenation reactions [18–21], but research focusing on hydrotreating has been carried out only recently [7–15].

It has been found that transition-metal phosphides can be easily synthesized by temperature-programmed reduction (TPR) of oxidic precursors (metal phosphates) at moderately high temperatures (773–873 K) [8]. Previous work has shown that MoP, WP, and Ni_2P have good activity in hydroprocessing [8,22–24], with overall activity in the following order: $Fe_2P/SiO_2 < CoP/SiO_2 < MoP < WP < Ni_2P/SiO_2$ in the HDS of dibenzothiophene (3000 ppm S) and in the HDN of quinoline (2000 ppm N) at 643 K and 3.1 MPa, with the comparison based on equal sites (240 μmol CO/O_2 for phosphides/sulfides) loaded in the reactor. A study of the effect of phosphorus content on Ni_2P/SiO_2 catalysts found that samples with excess P (initial Ni/P ratio $= 1/2$) gave more dispersed and stable phases with higher activity (dibenzothiophene HDS conversion of 100% and quinoline HDN conversion of 81% at a liquid hourly space velocity [LHSV] of 0.65 h^{-1}) [24]. Recently, the structure, synthesis, and reactivity of phosphide catalysts were reviewed [17].

Better knowledge of the surface and catalytic properties of the supported phosphide catalysts will help enhance the activity and stability of phosphides for treating heavier feeds. In this work we focused on investigating the structural and chemisorption properties of the supported Ni_2P catalysts. We used extended X-ray absorption fine structure (EXAFS) spectroscopy to study the atomic arrangement in the finely dispersed phosphide phases and Fourier transform infrared (FTIR) analysis to study the chemisorption of CO and pyridine on their surfaces. Previous work focused on the activity of Ni_2P in the HDS of thiophene [1] and dibenzothiophene [16,23–26]. In this study that work is extended to the HDS of 4,6-DMDBT, investigating the effect of N compounds on HDS conversion and tetralin hydrogenation. The Ni_2P/SiO_2 catalyst and a commercial Ni–Mo–S/Al_2O_3 catalyst are compared.

2. Experimental

2.1. Catalyst and reference samples

The supported Ni_2P catalyst was prepared as reported previously with excess phosphorus ($Ni/P = 1/2$) and a loading of 1.156 $mmol_{Ni}\,g_{support}^{-1}$ (12.2 wt% Ni_2P/SiO_2) using a commercial SiO_2 support (Cabot, Cab-O-Sil) of high surface area (EH-5, 350 $m^2\,g^{-1}$) [24,27]. A supported nickel phosphate precursor was prepared by incipient wetness impregnation of a solution of nickel nitrate [$Ni(NO_3)_2$, Alfa Aesar] and ammonium phosphate [$(NH_4)_2HPO_4$, Aldrich], followed by drying at 393 K for 6 h and calcination at 673 K for 4 h. The supported nickel phosphate was then reduced to a phosphide by TPR from 298 to 883 K (at a rate of 1 $K\,min^{-1}$). The hydrogen flow rate was set at 1000 $μmol\,s^{-1}$ [1500 cm^3(NTP) min^{-1}] per g of sample. At the end of the temperature program, the sample was cooled to room temperature in helium and passivated under 0.5% O_2/He for 6 h.

Reference NiO/SiO_2 and PO_x/SiO_2 samples were prepared by impregnation of the SiO_2 support (Cabot, Cab-O-Sil, EH-5, 350 $m^2\,g^{-1}$) with nickel nitrate [$Ni(NO_3)_2$, Alfa Aesar] (1.16 $mmol_{Ni}\,g_{support}^{-1}$) and $(NH_4)_2HPO_4$ (2.3 $mmol_P\,g_{support}^{-1}$), followed by drying at 393 K for 6 h and calcination at 673 K for 4 h. The calcined NiO/SiO_2 sample was then reduced at 673 K for 2 h to form a Ni/SiO_2 sample or was sulfided in a 10% H_2S/H_2 carrier at 673 K for 2 h to form a sulfided NiS/SiO_2 sample. A bulk Ni_2P (Cerac, 99.5%) reference was used for comparison to experimental EXAFS results. The sulfide catalyst was a commercial Ni–Mo–S/Al_2O_3 sample (Criterion 424) containing approximately 15 wt% MoO_3, 3 wt% NiO, and some phosphorus promoter. Typical phosphorus content for commercial catalysts is 2–4 wt% [28].

2.2. Characterization of samples

X-Ray diffraction (XRD) patterns of both the freshly prepared and spent samples were obtained with a Scintag XDS-2000 powder diffractometer operated at 45 kV and 40 mA using Cu-K_α monochromatized radiation ($\lambda = 0.154178$ nm). CO chemisorption uptakes were obtained on passivated, air-exposed samples rereduced in hydrogen for 2 h at 723 K, and used to calculate needed catalyst quantities in the hydroprocessing tests. Pulses (20 μmol) of CO at room temperature (300 K) were passed over the sample to measure the total dynamic gas uptake. A Micromeritics ASAP 2010 micropore size analyzer was used to measure the specific surface area of the sample from the linear portion of BET plots ($P/P_0 = 0.01$–0.10) at 77 K. Before the measurements, the passivated samples were degassed at 403 K for 12 h. The chemical composition of the samples was determined by inductively coupled plasma–absorption emission spectroscopy (Spectro Analytical Instruments, Spectroflame FTMO A85D). For complete dissolution of the samples, aqua regia digestion was carried out with heating in a microwave oven (EthosPlus, Milestone).

X-Ray absorption spectra at the Ni K-edge (8.333 keV) of reference and catalyst samples were recorded in the energy range 8.233–9.283 keV at beam line X18B at the National Synchrotron Light Source at Brookhaven National Laboratory. The X-ray ring at the National Synchrotron Light Source has a flux of 1×10^{10} photons s^{-1} at 100 mA and 2.5 GeV. The monochromator is equipped with a Si(111) channel-cut single crystal and has an energy range capability of 5.8–40 keV. The crystal was detuned slightly to prevent glitches due to harmonics. EXAFS spectra were recorded at ambient temperature in transmission mode using ionization chambers for the detection of primary (I_0, 100% N_2) and transmitted (I_t, 75% N_2, balance Ar) beam intensities. Bulk reference samples were diluted with BN (0.1 g_{cat} + 0.3 g_{BN}). The EXAFS data were analyzed by Winxafs 97. To fit the experimental EXAFS spectra for the fresh and spent samples, the theoretical EXAFS equation for Ni_2P was used to calculate phase shifts and amplitude functions of Ni_2P, using FEFF (version 8.20) [29]. Fitting was then carried out for the fresh samples using the three dominant shells (2 Ni–P at 0.2266 nm, 4 Ni–P at 0.2457 nm, and 4 Ni–Ni at 0.2678 nm), using a reducing factor (S_0^2), fixed as 0.90, a value obtained by fitting the Ni–Ni contribution in Ni foil. The quality of the fit was evaluated by the residual factor (R-factor), which is defined by

$$\text{Residual factor (R-factor, \%)} = \left(\frac{\sum_{i=1}^{N} |y_{\text{exp}}(i) - y_{\text{theo}}(i)|}{\sum_{i=1}^{N} y_{\text{exp}}(i)} \right) \times 100,$$

where y_{exp} and y_{theol} are experimental and theoretical data points, respectively.

Transmission infrared spectra of pressed wafers (~15 mg) of Ni_2P/SiO_2 and Ni–Mo–S/Al_2O_3 catalysts were collected in situ in an infrared (IR) reactor cell placed in a FTIR spectrometer (Bio-Rad Model FTS 3000MX) at a resolution of 2 cm^{-1} and using 64 scans $spectrum^{-1}$. The IR cell was equipped with KBr windows, connections for inlet and outlet flows, and thermocouples connected to a temperature controller to monitor and control the temperature. Before dosing CO and pyridine, the Ni/SiO_2 and Ni_2P/SiO_2 samples were reduced in H_2 at 723 K for 2 h, and the NiS/SiO_2 and Ni–Mo–S/Al_2O_3 samples were sulfided in a 10% H_2S/H_2 stream at 673 K for 2 h at a flow rate of 100 $\mu mol\,s^{-1}$ (150 $cm^3\,min^{-1}$). For the CO IR measurements, the samples after pretreatment were cooled to room temperature in a He flow and exposed to 1% CO/He until saturation was achieved. The samples were then purged in He carrier for 300 s to remove gaseous and weakly adsorbed CO species. The spectra were obtained in the absorbance mode and are shown after subtraction of a background spectrum obtained on the samples before adsorption to make the adsorbate peaks more clear. For pyridine adsorption, the samples were dosed at 373 K with a molar concentration of pyridine of 0.40% in a He or H_2 carrier at a flow rate of 100 $\mu mol\,s^{-1}$ (150 $cm^3\,min^{-1}$) until saturation was achieved. The samples were then purged in He for 300 s at 373 K to remove the gaseous and weakly adsorbed pyridine. The spectra are shown after substraction of the background spectrum obtained at the various temperatures without pyridine. Measurements were made at 373, 423, 473, 523, and 573 K, with the temperature raised at a rate of 0.17 $K\,s^{-1}$ (10 $K\,min^{-1}$) and a hold time of 180 s maintained at each temperature.

2.3. Activity test for HDS

Catalytic activities for the HDS of 4,6-DMDBT, the HDN of quinoline, and the hydrogenation of tetralin were carried out at 3.1 MPa (450 psig) at 573 K (300 °C) in a three-phase upflow fixed-bed reactor. The feed liquid was prepared by combining 1% tetralin (Aldrich, 99%), 0% or 0.02% N as quinoline (Aldrich, 99%), 0.05% S as 4,6-DMDBT (Fisher, 95%), 0.3% S as dimethyldisulfide (DMDS, Aldrich, 99%), 1% *n*-octane (Aldrich, 99%) as an internal standard, and *n*-tridecane (Alfa Aesar, 99%) as a solvent. The liquid was delivered at 0.0833 $cm^3\,s^{-1}$ (5 $cm^3\,h^{-1}$) using a liquid pump along with 100 $\mu mol\,s^{-1}$ [150 cm^3(NTP) min^{-1}] of hydrogen flow. Liquid product compositions were determined with a Hewlett Packard 5890A gas chromatograph, equipped with a 50-m, 0.32-mm-i.d. dimethylsiloxane column (Chrompack, CPSil 5B), on samples collected at 4- to 5-h intervals. Reaction products were identified by gas chromatography–mass spectroscopy (HP5972) analysis. Quantities of catalysts loaded in the reactor corresponded to the same amount of CO or atomic oxygen uptake (240 µmol), and were 2.3 g for the Ni_2P/SiO_2 catalyst, and 0.83 g for the Ni–Mo–S/Al_2O_3 catalyst, with corresponding LHSV of 0.80, and 4.0 h^{-1}. Before the hydroprocessing reaction, the passivated phosphide catalysts were pretreated for 2 h at 623 K in 100 $\mu mol\,s^{-1}$ [150 cm^3(NTP) min^{-1}] of H_2, and the sulfide catalyst was pretreated at 578 K for 2 h under 100 $\mu mol\,s^{-1}$ of 10% H_2S/H_2 at a pressure slightly above 1 atm. The HDS of 4,6-DMDBT proceeded via two reaction pathways, direct desulfurization (DDS) and hydrogenation (HYD) followed by desulfurization. The DDS pathway gave 3,3-dimethylbiphenyl (3,3-DMBP), and the HYD pathway formed methylcyclohexyltoluene (MCHT) and dimethylbicyclohexane (DMBCH). The products of the quinoline reaction were primarily the denitrogenated molecules propylbenzene and propylcyclohexane. The products of hydrogenation of tetralin were the dehydrogenated (deHYD) molecule naphthalene and the hydrogenated (HYD) molecule decalin.

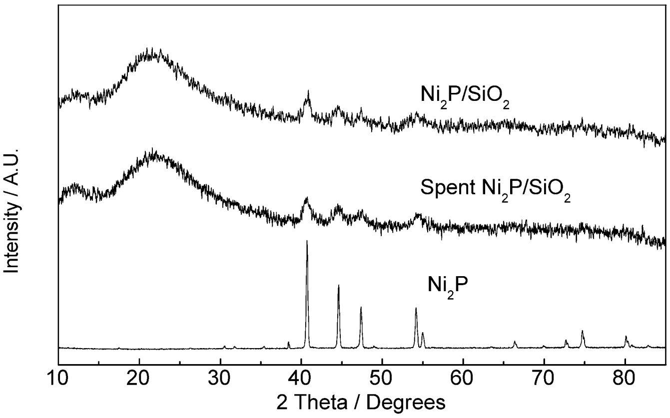

Fig. 1. XRD patterns of fresh and spent Ni_2P samples.

Table 1
Physical properties of Ni_2P, Ni/SiO_2, and NiS/SiO_2

	CO uptake ($\mu mol\,g^{-1}$)	BET area ($m^2\,g^{-1}$)	Ni/P molar ratio
Ni_2P/SiO_2	112	240	1/0.963
Ni/SiO_2	17	139	–
NiS/SiO_2	3	144	–

3. Results

3.1. Structural features of Ni_2P catalyst

Fig. 1 shows the powder XRD patterns of the fresh and spent Ni_2P catalyst, as well as a bulk Ni_2P reference. The XRD patterns confirm that a Ni_2P phase is formed on the SiO_2 support and that the phase is retained during the reaction. The physical properties of the Ni_2P/SiO_2 catalyst are listed in Table 1.

Fig. 2 shows the hexagonal structure of Ni_2P. The Ni_2P unit cell has two types of Ni and P sites [denoted as Ni(I), Ni(II) and

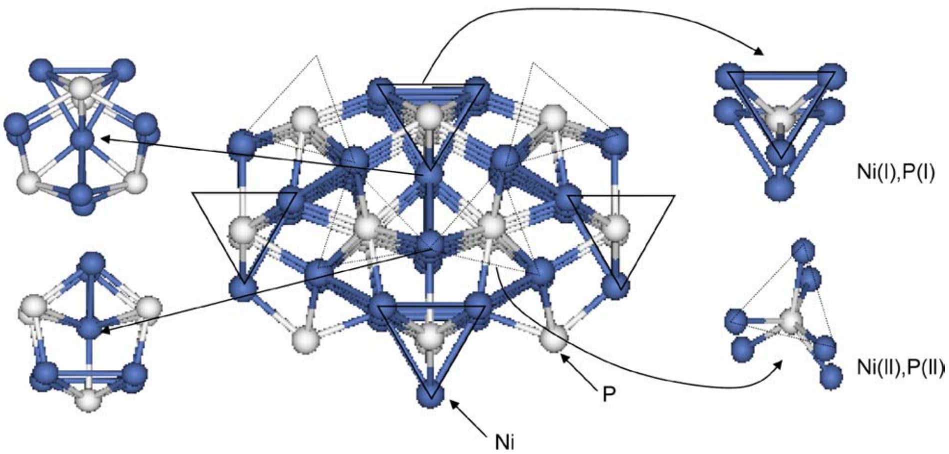

Fig. 2. Local structure of Ni_2P with two types of trigonal prisms.

Table 2
Curve-fitting results of the Ni K-edge EXAFS spectra for the bulk Ni_2P sample[a]

Parameter	Ni–P				Ni–Ni			R-factor (%)
	Ni(I)–P(II)	Ni(I)–P(I)	Ni(II)–P(I)	Ni(II)–P(II)	Ni(I)–Ni(II)	Ni(I)–Ni(I)	Ni(I)–Ni(II)	
Ni_2P reference coordination number (CN)	2	2	1	4	2	2	4	
Ni_2P reference bond length (R)	0.2209	0.22662	0.23688	0.24567	0.2605	0.26131	0.26783	
Fit 1								
CN		1.43					4.22	2.68
R (nm)		0.222					0.2618	
σ^2 (10^{-5} nm^2)		7.835					8.0466	
ΔE (eV)		−8.424					−2.192	
Fit 2								
CN		2.11	1.47			4.01		0.69
R (nm)		0.2237	0.2392			0.2646		
σ^2 (10^{-5} nm^2)		0.879	6.91			1.599		
ΔE (eV)		1.25	1.411			0.543		
Fit 3								
CN		2.01		1.75			3.99	0.48
R (nm)		0.2253		0.2401			0.2644	
σ^2 (10^{-5} nm^2)		3.00		0.499			6.00	
ΔE (eV)		0.420		0.423			1.798	
Fit 4								
CN		2.1	1.51				4.01	1.51
R (nm)		0.2248	0.2400				0.2649	
σ^2 (10^{-5} nm^2)		4.76	1.606				6.01	
ΔE (eV)		1.177	1.099				1.941	

[a] ΔR filtered $= 0.1427$–0.27598 nm, $S_0^2 = 0.9$, the unit cell contains equal numbers of Ni(I) and Ni(II) atoms.

P(I), P(II)], which form two different trigonal prisms consisting of various Ni–P and Ni–Ni subshells. The unit cell contains 3 Ni(I), 3 Ni(II), 1 P(I), and 2 P(II). Bond distance and coordination number for the subshells in each trigonal prism are listed in Table 2. EXAFS simulations were carried out taking each Ni site as the absorber in a 0.5-nm cluster to obtain phase shifts and effective scattering amplitudes from fitted data of the bulk Ni_2P reference and Ni_2P/SiO_2 sample.

Fig. 3 shows the Ni K-edge EXAFS spectra (left panels) after background subtraction and their Fourier transforms (right panels) of Ni/SiO_2 (Fig. 3A), sulfided NiS/SiO_2 (Fig. 3B), Ni foil (Fig. 3C), and a NiS reference (Fig. 3D). The first peaks in the Fourier transforms are centered at 0.215, 0.200, 0.217, and 0.202 nm, respectively. A reduction factor, S_0^2, of 0.9 for the absorber Ni atom was obtained from the spectrum of a Ni foil reference (not shown).

Fig. 4 shows a comparison between simulated and experimental EXAFS spectra for Ni_2P, with the left panels showing the EXAFS oscillation and the right panels showing the Fourier transforms. Fig. 4A shows the simulation for the absorber Ni(I), which gives two distinct peaks centered at 0.175 and 0.240 nm, corresponding to Ni–P and Ni–Ni contributions,

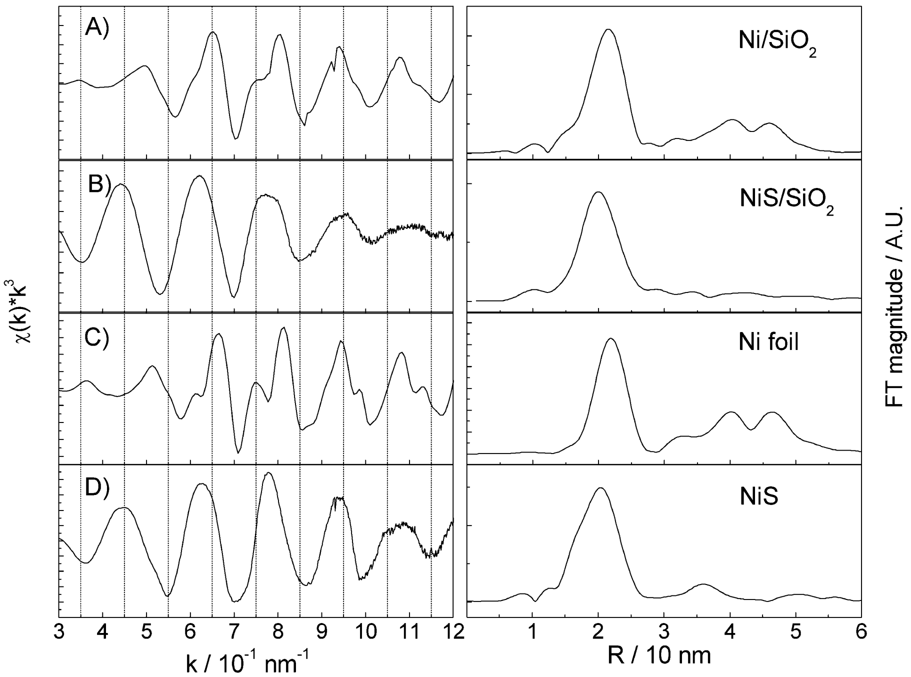

Fig. 3. Ni K-edge EXAFS spectra and Fourier transforms of Ni/SiO$_2$, NiS/SiO$_2$, Ni foil, and NiS references.

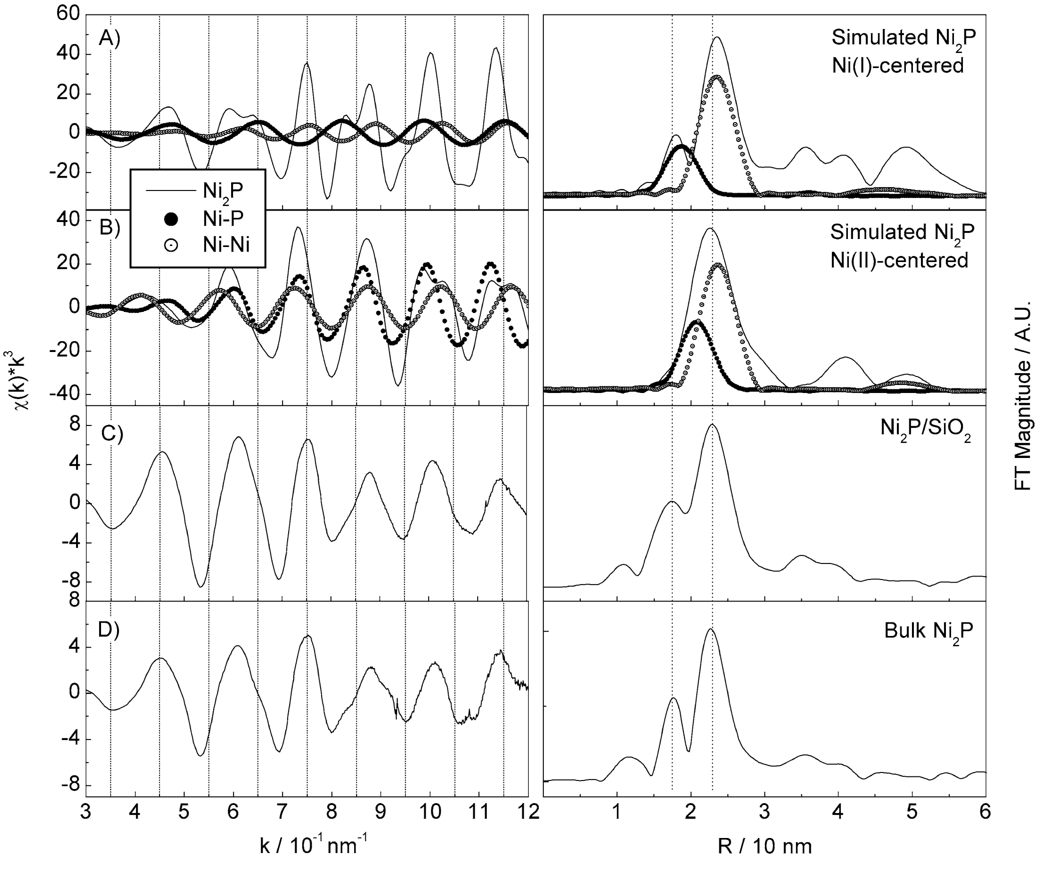

Fig. 4. Comparison of the Ni K-edge EXAFS spectra for simulated Ni$_2$P, bulk Ni$_2$P, and Ni$_2$P/SiO$_2$ samples.

respectively. Fig. 4B shows the simulation for the absorber Ni(II), which gives one broad peak centered at 0.225 nm, resulting essentially from two overlapping peaks due to Ni–P and Ni–Ni neighbors. Fig. 4C shows the results for Ni$_2$P/SiO$_2$ catalysts with the Fourier transform spectra exhibiting peaks at 1.74 and 2.27 nm. Fig. 4D shows simulation results for the bulk reference Ni$_2$P sample with the Fourier transform showing peaks at 1.75 and 2.25 nm.

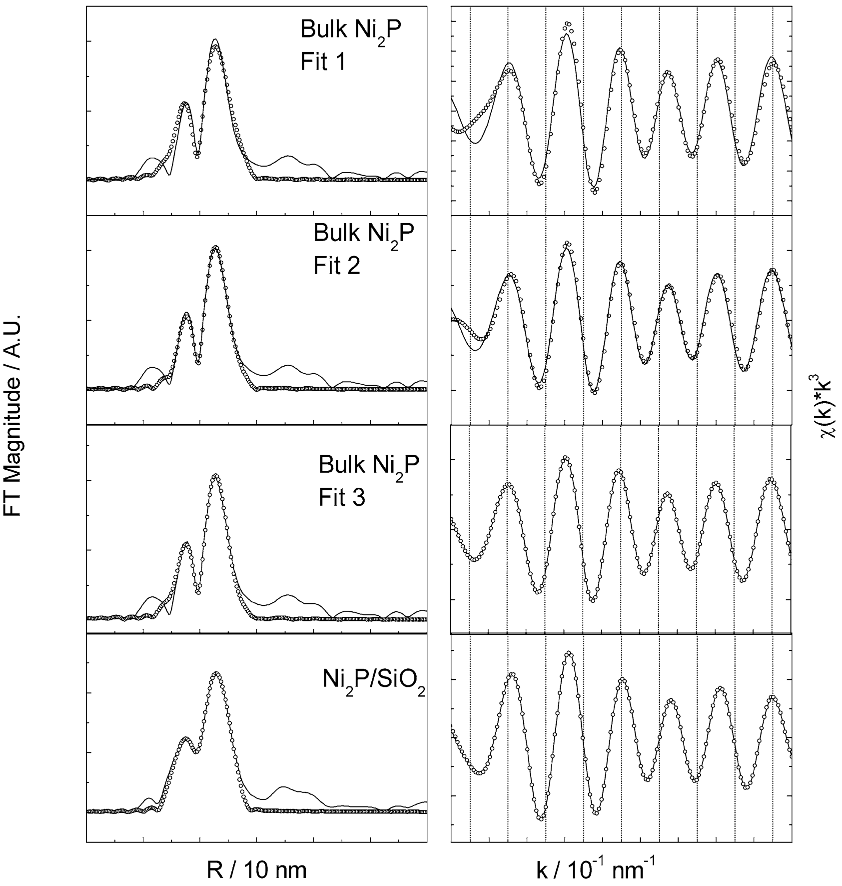

Fig. 5. Ni K-edge Fourier transforms and Fourier filtered EXAFS spectra of bulk Ni_2P and Ni_2P/SiO_2 samples.

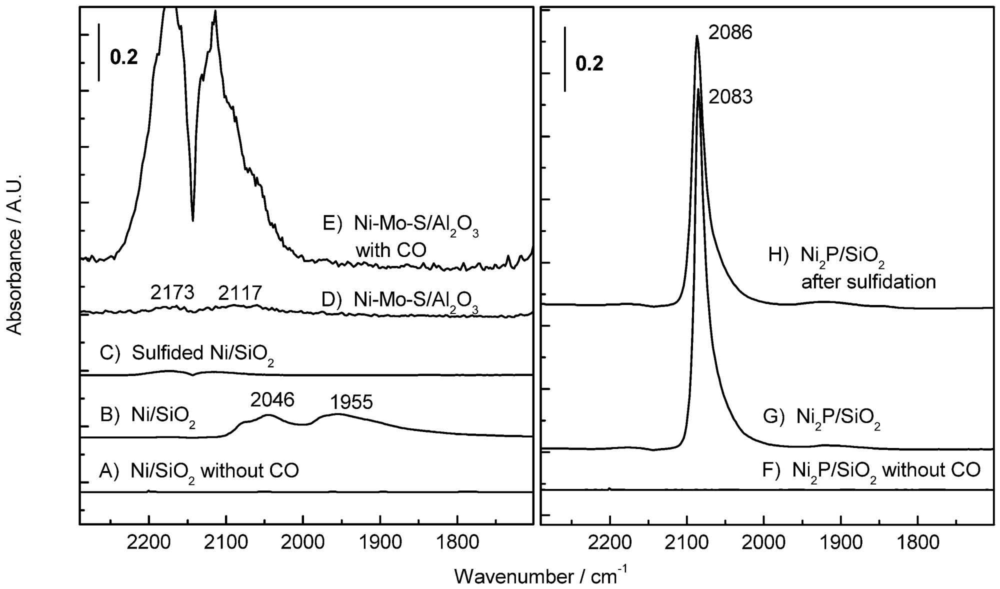

Fig. 6. FTIR spectra of adsorbed CO on Ni/SiO_2, sulfided NiS/SiO_2, $Ni–Mo–S/Al_2O_3$, and Ni_2P/SiO_2 samples.

Fig. 5 shows the curve-fitting results of the Ni K-edge EXAFS spectra for bulk Ni_2P and Ni_2P/SiO_2 samples with the left panels showing the Fourier transforms (solid line) and fits (open circles), and the right panels showing the EXAFS oscillations (solid line) and fits (open circles). The fitting parameters are given in Table 2.

3.2. Surface properties of the Ni_2P catalyst

Fig. 6 shows room temperature FTIR spectra of adsorbed CO in He flow on Ni/SiO_2, sulfided NiS/SiO_2, $Ni–Mo–S/Al_2O_3$, and Ni_2P/SiO_2 samples. All bands are due to the C–O stretch. Fig. 6A shows the IR spectrum before the introduction of CO

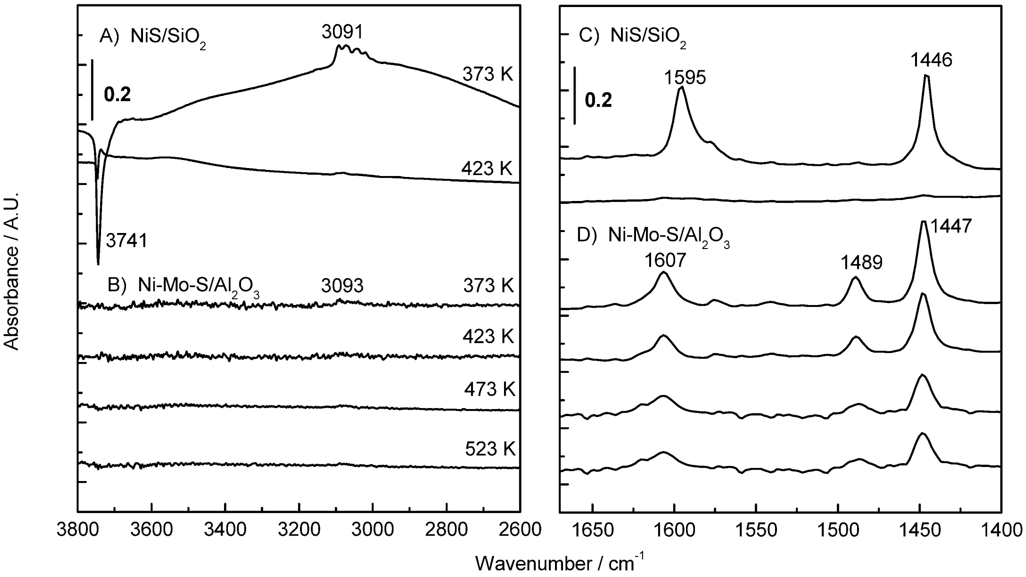

Fig. 7. FTIR spectra of adsorbed pyridine on Ni/SiO_2, sulfided Ni/SiO_2, and $Ni–Mo–S/Al_2O_3$ samples.

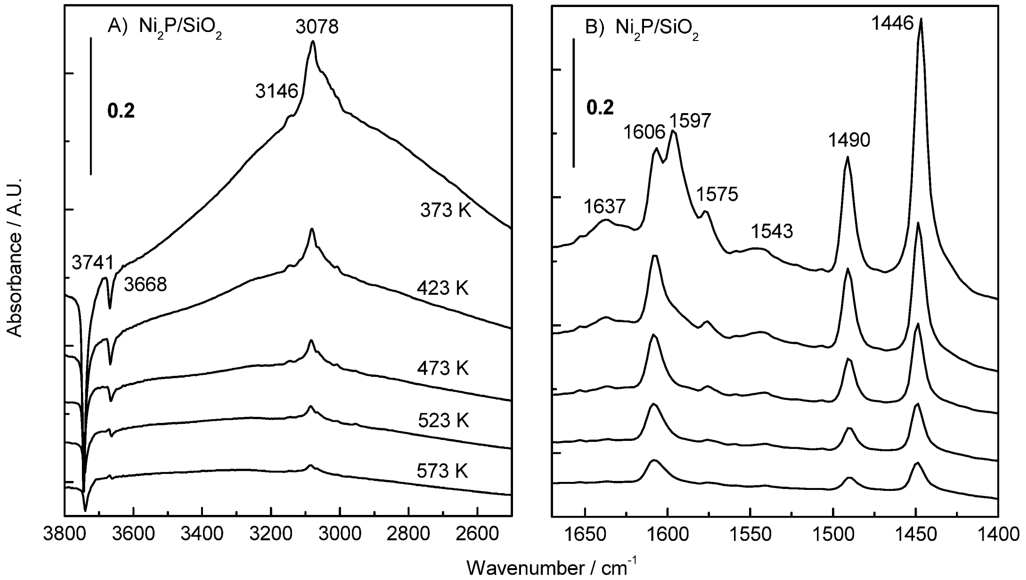

Fig. 8. FTIR spectra of adsorbed pyridine on the Ni_2P/SiO_2 sample.

for a Ni/SiO_2 sample, exhibiting no peak. Fig. 6B shows the IR spectrum of adsorbed CO on the Ni/SiO_2 sample, which gives two broads bands centered at around 2046 and 1955 cm^{-1}. Figs. 6C and 6D show the results for sulfided NiS/SiO_2 and $Ni–Mo–S/Al_2O_3$ samples, which give only traces of physisorbed CO species observed at 2173 and 2117 cm^{-1}. Fig. 6E shows the IR spectrum with CO saturation for the $Ni–Mo–S/Al_2O_3$ sample, which gives the peaks for the physisorbed CO species observed at 2173 and 2117 cm^{-1}. Fig. 6F shows the IR spectrum prior to the introduction of CO for a Ni_2P/SiO_2 sample, again showing no peak. Fig. 6G shows the IR spectrum of adsorbed CO on the Ni_2P/SiO_2 sample, which gives a distinctive IR band at 2083 cm^{-1}. Fig. 6H shows the result for the sulfided Ni_2P/SiO_2 sample (treated in a flow of 10% H_2S/H_2 at 673 K for 2 h), which retained the IR band at 2086 cm^{-1}, with the intensity being lowered.

Fig. 7 shows FTIR spectra in the high- and low-wavenumber regions of adsorbed pyridine in a He carrier for NiS/SiO_2 and $Ni–Mo–S/Al_2O_3$ samples after pretreatment in a flow of 10% H_2S/H_2 at 673 K for 2 h. The spectra were obtained after adsorption at 373 K and successive heating to various temperatures in a flow of He. For the sulfided Ni/SiO_2 sample, positive peaks centered at 3091 cm^{-1} (Fig. 7A), 1595 cm^{-1} and 1446 cm^{-1} (Fig. 7C) were observed, which decreased in intensity with increasing temperature. For $Ni–Mo–S/Al_2O_3$, peaks centered at 1607, 1489, and 1447 cm^{-1} (Fig. 7D) were observed, with no distinctive features found in the higher-frequency region (Fig. 7B). Again, the intensity of the peaks decreased on heating.

Fig. 8 shows FTIR spectra in the high- and low-wavenumber regions of adsorbed pyridine in a He carrier for the Ni_2P/SiO_2 catalyst. Again, the spectra were obtained after adsorption at

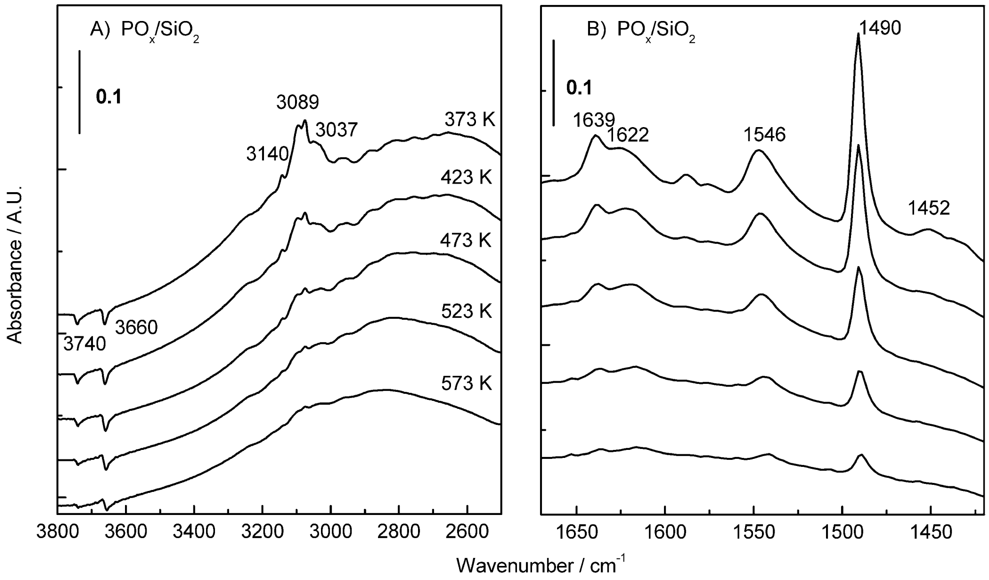

Fig. 9. FTIR spectra of adsorbed pyridine on the PO$_x$/SiO$_2$ sample.

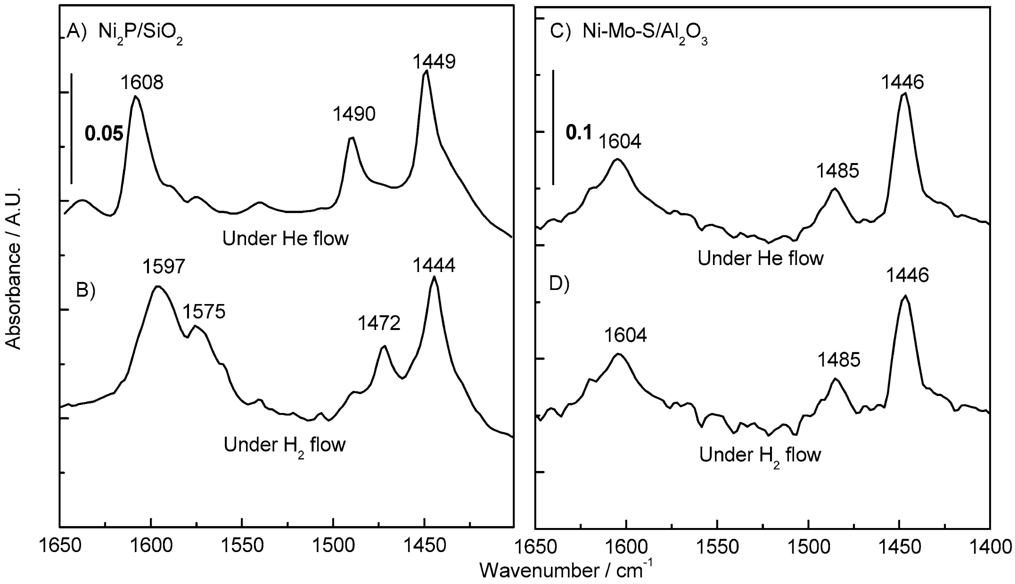

Fig. 10. In situ FTIR spectra of the hydrogenation of the pyridine at 573 K on Ni$_2$P/SiO$_2$ and Ni–Mo–S/Al$_2$O$_3$ samples.

373 K and successive heating to various temperatures in a flow of He. Positive peaks centered at 3146 and 3078 cm^{-1} (Fig. 8A) and at 1637, 1606, 1597, 1575, 1543, 1490, and 1446 cm^{-1} (Fig. 8B) were observed. Negative peaks at 3741 and 3668 cm^{-1} (Fig. 8A) due to hydroxyl groups were also present. An increase in the temperature led to a decrease in the intensity of the peaks.

Fig. 9 shows FTIR spectra of adsorbed pyridine in a He carrier for the PO$_x$/SiO$_2$ sample. Once again adsorption was carried out at 373 K, with subsequent sample heating. Positive peaks centered at 3140, 3089, and 3037 cm^{-1} (Fig. 9A) and at 1639, 1622, 1546, 1490, and 1452 cm^{-1} (Fig. 9B) were observed. Negative peaks at 3740 and 3660 cm^{-1} (Fig. 9A) due to hydroxyl groups were also visible. An increase of the temperature led to a decrease in the intensity of the peaks, with the peaks at 3660, 1546, and 1490 cm^{-1} retained up to 573 K.

Fig. 10 compares the FTIR spectra of pyridine adsorbed on the Ni$_2$P/SiO$_2$ (Fig. 10A) and Ni–Mo–S/Al$_2$O$_3$ (Fig. 10C) samples under He flow at 573 K. The behavior of the adsorbed species is also examined on these catalysts at 573 K on switching the carrier flow from He to H$_2$ (Figs. 10B and 10D). For the Ni$_2$P/SiO$_2$ sample, the main spectral features appeared at 1608, 1490, and 1449 cm^{-1} in He, but these shifted to bands at 1597, 1575, 1472, and 1444 cm^{-1} due to piperidine with the introduction of H$_2$. For the Ni–Mo–S/Al$_2$O$_3$ sample, the main spectral features appeared at 1604, 1485, and 1446 cm^{-1} in He. Unlike in the Ni$_2$P/SiO$_2$ sample, here switching the carrier from He to H$_2$ led to little change in the IR peaks.

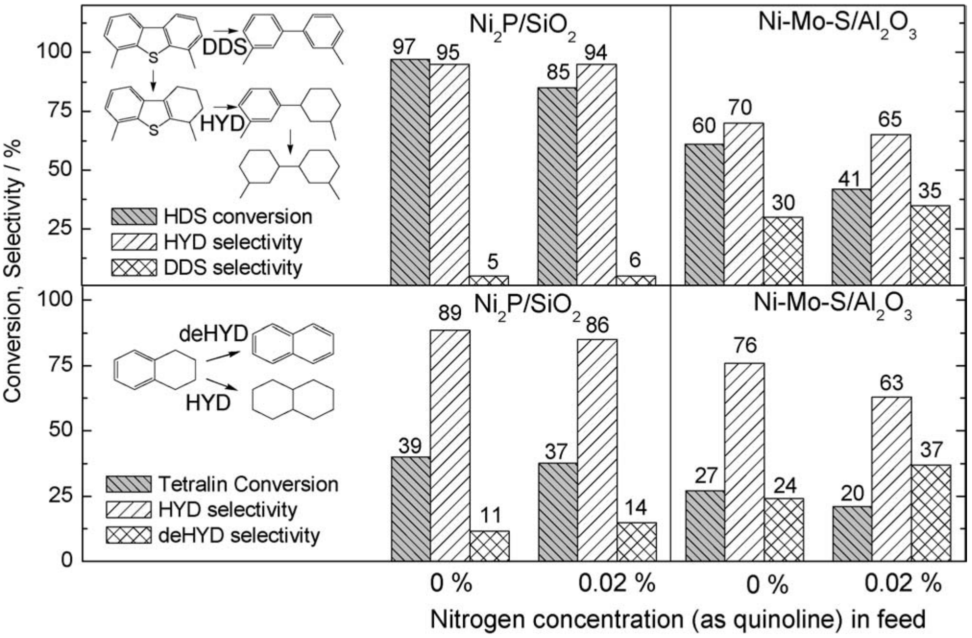

Fig. 11. Activities in the HDS of 4,6-DMDBT and hydrogenation of tetralin for Ni_2P/SiO_2 and Ni–Mo–S/Al_2O_3 at 613 K and 3.1 MPa.

3.3. *Catalytic activity in the HDS of 4,6-DMDBT*

Fig. 11 shows the HDS conversion of 4,6-DMDBT and the selectivities toward the HYD and DDS products for the Ni_2P/SiO_2 and NiMoS/Al_2O_3 catalysts at 613 K (340 °C) and 3.1 MPa at two levels (0 and 0.02%) of N content (as quinoline). Initially, the feed contained 4,6-DMDBT (0.05% S), DMDS (0.3% S), and tetralin (1%) dissolved in tridecane. For the Ni_2P/SiO_2 catalyst, the HDS conversion was high (97%), with an HYD selectivity of 95%, whereas for the NiMoS/Al_2O_3 catalyst, the HDS conversion was low (around 60%), with an HYD selectivity of 70%. The addition of N (0.02% N as quinoline) led to a decrease in HDS conversion from 97 to 85% for the Ni_2P/SiO_2 and from 60 to 41% for the Ni–Mo–S/Al_2O_3 catalyst. This was accompanied by a decrease in the HYD selectivity from 95 to 94% for the Ni_2P/SiO_2 catalysts and from 70 to 65% for the Ni–Mo–S/Al_2O_3 catalyst. Fig. 11 also displays the conversion of tetralin and its product selectivities. For the Ni_2P/SiO_2 catalyst, the tetralin conversion and HYD selectivity were around 39 and 89%, respectively, and the addition of N led to a slight decrease in these values to 37 and 86%. For the Ni–Mo–S/Al_2O_3 catalyst, the tetralin conversion and HYD selectivity were around 27 and 76%, respectively, and the addition of N led to a decrease in these values to 20 and 63%.

4. Discussion

4.1. *Structural properties of the Ni_2P/SiO_2*

Ni_2P [30] adopts a hexagonal structure (Space group: $P_{\bar{6}2m}$, D^2_{3h}, Struckturbericht notation: revised C22) with lattice parameters $a = b = 0.5859$ nm and $c = 0.3382$ nm, in which the Ni atoms form two types of nine-fold arrangements around each P atom (Fig. 2). Both nine-fold arrangements consist of a Ni trigonal prism around a P and three additional Ni atoms bonded to the center P through the three rectangular faces of the trigonal prism. The two types of Ni and P sites [denoted as Ni(I), Ni(II)) and P(I), P(II)] form two different trigonal prisms in Ni_2P. Such nine-fold arrangements are very common in metal-rich phosphides [31]. For example, the Ni(I) site is surrounded by 4 P atoms (2 P at 0.2209 nm and 2 P neighbors at 0.2266 nm) and 8 Ni atoms [2 Ni(I) at 0.2613 nm, 2 Ni(II) at 0.2605 nm, and 4 Ni(II) at 0.26783 nm]. The Ni(II) site is surrounded by 5 P atoms (1 P at 0.2369 nm and 4 P at 0.2457 nm) and 6 Ni atoms [2 Ni(I) at 0.2605 nm and 4 Ni(I) at 0.26783 nm]. Equal numbers of Ni(I) and Ni(II) atoms are present in the unit cell.

The XRD patterns of the fresh and spent Ni_2P/SiO_2 samples indicate that the main bulk phase on the catalyst was Ni_2P (Fig. 1), with line-broadening giving a crystallite size of 6.5 nm. This is in agreement with transmission electron microscopy images of a similar catalyst showing approximately 10-nm particles [26]. The sample was prepared by TPR in flowing hydrogen, which led to a loss of phosphorus during reduction and gave a lower amount of phosphorus (Ni/P ratio $= 1/0.963$) than the initial value (1/2). The surface area of the fresh Ni_2P/SiO_2 catalyst (240 $m^2\,g^{-1}$) was lower than that of the support (350 $m^2\,g^{-1}$) (Table 1), likely due to the agglomeration of support particles. Chemisorption quantities of CO for the fresh sample (112 $\mu mol\,g^{-1}$) were moderate and were retained during reaction [63]. The dispersion, defined as the fraction of surface metal atoms, can be calculated from the CO uptake as 9.7%. A 6.5-nm crystallite contains about 2300 unit cells and 23,000 Ni atoms. Based on the crystal structure and a surface atom density of $1.01 \times 10^{15}\ cm^{-2}$ [23], this corresponds to a dispersion of 10.4%, which is in good agreement with the value calculated from the CO uptake.

The XRD patterns of the catalysts (Fig. 1) demonstrated low signal-to-noise ratios and do not yield detailed structural information. EXAFS analysis is particularly useful for charac-

Table 3
Comparison of curve-fitting results of the Ni K-edge EXAFS spectra for the bulk Ni_2P reference and the Ni_2P catalyst[a]

Samples	Ni–P								Ni–Ni (I,II)				R-factor (%)
	Ni(I)–P(I)				Ni(II)–P(II)								
Reference parameter	CN	R (nm)	σ^2 (10^{-5} nm^2)	ΔE (eV)	CN	R (nm)	σ^2 (10^{-5} nm^2)	ΔE (eV)	CN	R (nm)	σ^2 (10^{-5} nm^2)	ΔE (eV)	
	2	0.2209			1	0.2369			2	0.2605			
	2	0.2266			4	0.2457			2	0.2613			
									4	0.2678			
Ni_2P (bulk)	2.0 ± 0.1	0.2253 ± 0.0002	3.0 ± 0.5	0.420	1.7 ± 0.2	0.2401 ± 0.0002	0.4 ± 0.5	0.42	4.0 ± 0.1	0.2644 ± 0.0002	6.0 ± 0.5	1.80	0.48
Ni_2P/SiO_2	1.9 ± 0.1	0.2225 ± 0.0003	6.4 ± 0.5	−4.260	3.2 ± 0.3	0.2383 ± 0.0003	8.4 ± 0.5	−4.26	3.0 ± 0.1	0.2625 ± 0.0002	8.1 ± 0.5	−1.15	1.048

[a] ΔR filtered = 0.1427–0.27598 nm, $S_0^2 = 0.9$.

terizing such dispersed phases on supports with large surface areas. Comparisons are made with bulk Ni (Fig. 3) and Ni_2P (Fig. 4) reference samples. Fourier transform EXAFS spectra for the Ni_2P/SiO_2 catalyst show two overlapping peaks in the 0.15–0.30 nm region (Fig. 4C), corresponding roughly to Ni–P and Ni–Ni bonds. For a quantitative analysis, it was impossible to extract directly from the experimental spectra the phase shifts and backscattering amplitude functions needed for the fits, because of insufficient separation of the peaks corresponding to the Ni and P neighbors and the possible superposition in the second shell of the Ni and P contributions. Therefore, the spectrum of the Ni_2P reference compound was first simulated using FEFF with structural parameters obtained from the literature [30]. Two separate EXAFS simulations were carried out, taking the Ni(I) and Ni(II) atoms to be absorbers in 0.5-nm Ni_2P clusters. The value of the reduction factor ($S_0^2 = 0.9$) for the absorber Ni atom was obtained from the curve fitting of the Ni K-edge EXAFS spectrum for a Ni foil reference (Fig. 3) and was used for the simulations of the bulk and Ni_2P catalyst samples. As shown in Fig. 4, the calculated Fourier transform for the Ni_2P with Ni(I) as the absorber exhibited the dominant features of the 4 phosphorus neighbors (2 at 0.2209 nm and 2 at 0.2266 nm) and the 8 nickel neighbors (2 at 0.2605 nm, 2 at 0.2613 nm, and 4 at 0.2678 nm), respectively. This allows us to understand the details of the experimental spectrum, which confirms that the first peak, centered at 0.181 nm, is due to a Ni–P bond and the second peak, centered at the longer distance of 0.234 nm, is due mainly to a Ni–Ni bond. The simulated Fourier transform for the Ni_2P with Ni(II) as the absorber gave rise to a broad peak centered at 0.2249 nm, in which two dominant features can be observed, the 5 phosphorus neighbors (1 atom at 0.2368 and 4 atoms at 0.2456) and 6 nickel neighbors (2 at 0.2605 nm and 4 at 0.2678 nm). The broad feature of this long-distance peak thus comprises both Ni–P and Ni–Ni contributions.

The contributions from the two nickel absorbers were used to fit the experimental EXAFS spectrum for the bulk Ni_2P. Because the number of independent fitting parameters is limited by 12 as given by the formula [32], $N_{\text{ind}} = 2 \cdot \Delta k \cdot \Delta R/\pi + 2$, a three-shell analysis, which uses nine parameters, is permissible. Various combinations of subshells, using two- and three-shell methods, were applied to obtain the best fit (Fig. 5). The two-shell method used one type of Ni–P shell and one type of Ni–Ni shell (fit 1). In the Ni–P shell, two P(I) neighbors at 0.2266 nm were used; in the Ni–Ni shell, 4 Ni(I,II) neighbors at 0.26783 nm were used. The three-shell method used two types of Ni–P shells and one type of Ni–Ni shell. In the first Ni–P shell, two P(I) neighbors at 0.2266 nm were used. In the second Ni–P shell, either one P(II) neighbor at 0.23688 nm or 4 P(II) neighbors at 0.24567 nm were used and compared (fits 2 and 3). In the Ni–Ni shell, either 2 Ni(I) neighbors at 0.26131 nm or 4 Ni(I,II) neighbors at 0.26783 nm were used and also compared (fits 3 and 4).

Table 2 summarizes the structural parameters of the Ni_2P reference sample [27] and compares the curve-fitting results of the two-shell (fit 1) and three-shell methods (fits 2–4). As explained above, various combinations of subshells were used to obtain the best fit in both cases. The three-shell method showed a better R-factor with more reasonable parameters than the two-shell method. For bulk Ni_2P, the coordination numbers of the first a Ni(I)–P shell and the third Ni–Ni(I,II) shell were in good agreement with those of the Ni_2P reference, with slightly lower bond lengths in both cases. The coordination number of the second shell of Ni(II)–P was close to 1, and the bond length was between the values of the two different types of P neighbors. Note that different combinations of fitting shells in the three-shell method produced little change in the parameters, characteristic of the averaging nature of EXAFS. For fit 3 in Table 2 in the first shell of Ni–P, the lower bond length (0.2253 nm) was due to the 2 P next-nearest neighbors at 0.2209 nm. In the second shell of Ni–P, the lower coordination number (1.750) and bond length (0.2401 nm) were due to the presence of the 1 P next-nearest neighbor at 0.23688 nm. In the third shell of Ni–Ni, the lower bond length (0.2644 nm) was due to the 2 Ni next-nearest neighbors at 0.26131 nm. Even though various combinations of the fitting reference shells were used, the resulting parameters displayed only small differences. These results imply that the three-shell analysis is effective for estimating the structural parameters.

The three-shell method was also applied for the Ni_2P/SiO_2 sample (using fit 3). Table 3 summarizes the curve-fitting results of the EXAFS spectra for the bulk Ni_2P sample and the freshly prepared Ni_2P sample. For Ni_2P/SiO_2 in the first shell, the Ni(I)–P(I) coordination number remained constant at around 1.9, with a decreased bond distance. In the second shell, the

Ni(II)–P(II) coordination number was much higher, at 3.19, with a lower bond distance compared with that of the bulk Ni_2P (0.2383 vs. 0.2401 nm). In the third shell, a decrease in the Ni–Ni(I,II), coordination number and bond length can be observed. In general, supported transition-metal catalysts show decreased coordination numbers and bond lengths compared with bulk samples, indicating atomic contraction in the dispersed particles [33]. Similar results were observed for the Ni_2P/SiO_2 sample, which had shorter bond lengths in all of the shells compared with bulk Ni_2P. The fitting results for the coordination numbers show an increase for the second shell of Ni(I)–P(II) and a decrease in the third shell of Ni–Ni. These results are likely due to the presence of extra P on the surface of the Ni_2P particles. A study of the effect of Ni/P ratio in the preparation of supported Ni_2P catalysts has shown that higher P is required to obtain highly active and stable catalysts [23]. The introduction of extra P in the preparation is important and was also carried out in this work. Elemental analysis confirms that there is extra P with a Ni/P ratio of 1/0.963 (Table 1). Comparison to the stoichiometric Ni/P ratio of 1/0.5 indicates a 48% P excess, although a portion of this probably resides on the support as unreduced phosphate. The increased coordination number in the second shell of Ni–P implies that the extra P affects the Ni–Ni coordination. Similar features were found in Mo_2N, suggesting that the extra N could be interstitially located in Mo_2N and could deform the Mo–Mo coordination [34]. A study of the effect of dispersion of Ni_2P catalysts supported on a high-surface area support (Si-MCM-41) has shown that high dispersion in Ni_2P results in stronger interactions between Ni and P, resulting in a higher coordination number in the second shell of Ni–P and a higher P/Ni molar ratio after the reduction [63]. It was also suggested that the extra P could reduce the Ni–Ni coordination, as was found here. The larger Debye–Waller factor in the experimental sample is likely due to disorder in the smaller particles.

4.2. Surface properties of the Ni_2P/SiO_2

Studies of CO adsorption are useful for characterizing the bonding properties of transition metal species [35–37]. Typically, the IR bands for M^{n+}–CO surface complexes are observed in the wavenumber region 2220–2000 cm^{-1}. For linearly adsorbed CO species on Ni cations, four main vibrational regions are found depending on the oxidation state of the Ni. Carbonyl complexes assigned to Ni^{3+}–CO and Ni^{2+}–CO give rise to respective IR bands at around 2155 and 2136 cm^{-1}, which are detected only at low temperatures and are easily removed by evacuation at room temperature [36]. The high frequency of vibration and the low stability of the complexes indicate that CO is bonded mainly by an electrostatic interaction and/or a σ bond to the Ni ion. Carbonyl complexes assigned to Ni^{+}–CO and Ni^{0}–CO give rise to IR bands at around 2130 and 2065 cm^{-1}, respectively, that are relatively stable and persist after evacuation at room temperature [37,38]. The low frequency of the vibration and the high stability suggests the presence of π back-bonding due to the higher d-electron density of the Ni species with a lower oxidation state.

For the Ni/SiO_2 sample, IR bands (Fig. 6) were observed at relatively low frequency, 2046 and 1955 cm^{-1}, and were assigned to linearly adsorbed and bridging CO species, respectively [34]. After treatment in 10% H_2S/H_2 at 673 K for 2 h, the IR bands disappeared, indicating that the sulfided Ni metal was not able to chemisorb CO. Similar to the sulfided NiS/SiO_2, the sulfided Ni–Mo–S/Al_2O_3 showed very weak IR peaks (at 2173 and 2117 cm^{-1}) due to physisorbed CO species on cationic sites, as found in previous studies [39–41]. Only at a very low temperature (140 K) did IR bands appear at 2125 cm^{-1} with low intensity [34,42], indicating a low electron density on the adsorbing metal sites. In contrast to these samples, the Ni_2P/SiO_2 gave a distinctive and stable IR band at 2086 cm^{-1}. After sulfidation, the peak reappeared at slightly higher frequency of 2083 cm^{-1} with diminished intensity. This effect, observed previously on another study on Ni_2P/SiO_2 [1,2], was attributed to weakening of the Ni–CO bond by electron withdrawal by sulfur. This frequency fell in the region between that of Ni^{+}–CO and Ni^{0}–CO, indicating the presence of π back-bonding in a low oxidation state. In addition, the IR band for bridging CO species was not observed, which is understandable because the bond distance given by EXAFS between Ni–Ni in Ni_2P is not close enough to form bridging CO groups compared with that in Ni metal. Similar results are found for noble metals in a low oxidation state, such as Pt and Pd, which are well known hydrogenation catalysts and display stable IR bands at low frequency ($\sim$2010 cm^{-1}) at room temperature [34,43]. The noble metals are significantly deactivated in an S environment, with a loss of active sites, however [44].

FTIR studies of pyridine adsorption as a function of temperature on the catalysts and reference samples were carried out to characterize the surface acidic properties. Pyridine is a good probe molecule because it can coordinatively bond to Lewis acid sites or can be protonated on Brønsted acid sites, with the pyridine ring vibrations modified in a characteristic manner [42]. For example, the CC(N) vibration mode ν_{19b} of the pyridine ring gives rise to wavenumbers at 1439, 1450, or 1545 cm^{-1} depending on whether the molecule is physisorbed, adsorbed on Lewis acid sites, or on Brønsted acid sites [45]. For reduced Ni/SiO_2, the adsorption of pyridine gave rise to IR bands at 3741, 3091, 1595, and 1446 cm^{-1} at 373 K (Fig. 7). The positive peaks at 3091, 1595, and 1446 cm^{-1} correspond to the vibration modes, ν_7(CH), ν_{8a}[CC(N)], and ν_{19b}[CC(N)] of the pyridine ring. The negative peak at 3741 cm^{-1} corresponds to an O–H stretching vibration mode on SiO_2 [46]. Because a background spectrum is substracted from all spectra, the decrease in the negative peaks indicates recovery in the O–H concentration with temperature. Initially, the O–H bond on Si–OH is strongly perturbed by its interaction with pyridine, but as the pyridine desorbs, the OH concentration rises again. The O–H feature returns to normal (zero intensity) on heating to 423 K, indicating that the pyridine is only weakly adsorbed on the Ni/SiO_2. For sulfided Ni–Mo–S/Al_2O_3 the pyridine adsorption gives rise to IR bands at 1607, 1489, and 1447 cm^{-1} at 373 K, and no distinctive peak is found in the higher frequency region (3800–2500 cm^{-1}). The peaks at 1489 and 1447 cm^{-1} correspond to the CC(N) vibration mode ν_{19b} of the pyridine ring and are indicative of the presence of Lewis acid sites due to Al sites on the Al_2O_3 support [47]. These peaks gradually disappear on heating to 523 K, indicating that pyridine is held with moderate strength on these sites on the Al_2O_3 support.

For reduced Ni_2P/SiO_2, the adsorption of pyridine gives rise to IR bands at 3741, 3668, 3078, 1606, 1597, 1575, 1543, 1490, and 1446 cm^{-1} at 373 K (Fig. 8). The negative peaks at 3741 and 3668 cm^{-1} correspond to hydroxyl vibrations of SiO–H and PO–H, respectively [45]. The broad band at 3078 cm^{-1} corresponds to C–H vibrations in pyridine. The peaks at 1543, 1490, and 1446 cm^{-1} correspond to pyridinium ring vibration modes ν_{19b} of CC(N) on Brønsted acid sites, ν_{19a} of CC(N) on Brønsted and Lewis acid sites, and ν_{19b} of CC(N) on Lewis acid sites [46]. The small peak at 1543 cm^{-1} is assigned to adsorption on Brønsted acid sites, which, unlike in Ni–Mo–S/Al_2O_3, is probably due to the PO–H site, as also indicated by the decreased intensity of the band at 3668 cm^{-1}. The assignment of the PO–H group on the Ni_2P/SiO_2 and Ni–Mo–S/Al_2O_3 catalysts was addressed in a previous study [48], in which a FTIR analysis of 2-methylpiperidine adsorption indicated that a PO–H group on the Ni_2P phase could readily protonate 2-methylpiperidine and form 2-methylpiperidium ion, as was also found for Ni–Mo–S/Al_2O_3. The results here suggest that the acidity of the PO–H group on Ni_2P/SiO_2 is slightly higher than that on Ni–Mo–S/Al_2O_3. For PO_x/SiO_2, pyridine adsorption gives rise to IR bands at 3740, 3660, 3089, 1639, 1622, 1546, 1490, and 1452 cm^{-1} at 373 K (Fig. 9). Note that the peak at 1546 cm^{-1} assigned to adsorption on a Brønsted acid site is much stronger than the peak at 1452 cm^{-1} due to adsorption on a Lewis site, indicating that the Brønsted acidity (due to PO–H groups) is dominant over the Lewis acidity on PO_x/SiO_2. Also, the small intensity of the peak at 3740 cm^{-1} indicates that SiO–H groups are scarce on the surface. This implies that the PO_x is located on or close to the SiO–H site, as also discussed previously [47]. The peak assigned to the PO–H groups on PO_x/SiO_2 is observed at a lower frequency than that on Ni_2P/SiO_2 (3660 vs. 3668 cm^{-1}) and persists even after heating to 573 K, indicating a stronger acidity for PO_x/SiO_2 compared with Ni_2P/SiO_2.

In situ FTIR measurements in hydrogen flow were carried out to examine the hydrogenation ability of the Ni_2P and Ni–Mo–S/Al_2O_3 catalysts at 573 K (Fig. 10). Pyridine was adsorbed on freshly pretreated catalysts at 373 K; after heating to 573 K in helium, the flow was shifted to hydrogen. The FTIR spectra showed that after 180 s, adsorbed pyridine on the Ni_2P/SiO_2 was converted to piperidine, whereas on Ni–Mo–S/Al_2O_3 little change occurred in the spectrum. It is thus concluded that the Ni_2P/SiO_2 surface has two distinctive sites that are very close to each other and are active for protonation and hydrogenation. The Ni–Mo–S/Al_2O_3 has considerably less hydrogenation ability.

4.3. Catalytic activities of the Ni_2P/SiO_2

Recently, more stringent environmental regulations for reducing sulfur in transport fuels have highlighted attention on deep sulfur removal from crude oil. Consequently, the focus for much HDS research has moved to the most refractory sulfur compounds [50,52,53]. In diesel fuels, these are typically the sterically hindered DBTs, that is, DBTs with alkyl substituents in the 4- or 4,6-positions [49,50]. The 4,6-DMDBT molecule is typically some 10 times less reactive than DBT itself [51–53]. Considering that >99% of the refractory sulfur compounds must be desulfurized to reduce the current sulfur content of 500 ppm S to the new standards of 15 ppm S for the United States and Europe, effective desulfurization of alkyl-substituted DBTs is essential to achieving deep HDS.

Two reaction pathways for the HDS of alkylsubstituted DBT have been proposed. The direct desulfurization pathway (DDS route) leads to 3,3-DMBP, whereas the hydrogenation pathway (HYD route) forms 4,6-tetrahydro- and hexahydro-DMDBTs as intermediates, which are desulfurized to MCHT and DMBCH [54–57]. Standard HDN/HDS catalysts consist of MoS_2-type phases supported on γ-Al_2O_3 and promoted by Co or Ni. The conventional Co–Mo–S/Al_2O_3 catalysts desulfurize primarily via the direct desulfurization route, whereas Ni–Mo–S/Al_2O_3 catalysts, which exhibit higher hydrogenation activity, desulfurize via the hydrogenation route. But the Ni–Mo–S/Al_2O_3 catalysts exhibit lower HDS activity than the Co–Mo–S/Al_2O_3 catalysts, particularly in the presence of high concentration of aromatics and nitrogen compounds, due to the inhibition caused by those compounds [58]. For this reason, gas–oil refining currently operates mostly with Co–Mo–S/Al_2O_3 catalysts at moderate temperatures (340–360 °C) and pressures (3.0–5.0 MPa). Nonetheless, these conditions are unable to achieve the low sulfur specification of gas oil of less than 15 ppm S [57]. Increasing the temperature to achieve higher HDS rates causes degradation of the produced oil due to unwanted side reactions. Thus, the development of more effective HDS catalysts is urgently needed.

Studies were carried out with two different feeds at 573 K and 3.1 MPa. Initially, a feed containing 0.35% S (0.3% S as DMDS and 0.05% S as 4,6-DMDBT) and 1% tetralin in a tridecane solvent was used. The results are given in Fig. 11, which shows conversions and selectivities based on equal sites loaded in the reactor of the Ni_2P/SiO_2 and Ni–Mo–S/Al_2O_3 catalysts. The sites were titrated by CO chemisorption for the phosphide and O_2 chemisorption for the sulfide. The amount of CO uptake has been shown to track the activity of Ni_2P [27,59] and is reasonable. For Ni_2P/SiO_2 the HDS reaction proceeded via the HYD pathway (∼95%) with a high conversion of ∼97%. Introduction of a N compound (quinoline) lowered the HDS conversion by 12%, to 85%, with little change in HYD selectivity. The catalytic activity for tetralin shows that the HYD pathway was also dominant over the deHYD pathway (89% vs. 11%) and that again the activity was little affected by the N compound. Similar catalytic behavior was observed for Ni–Mo–S/Al_2O_3 but with a much lower HDS conversion, particularly in the presence of the N-compound. Ni–Mo–S/Al_2O_3 also demonstrated lower hydrogenation activity for tetralin than Ni_2P/SiO_2, with the N compound having a significant negative effect on the conversion. These results indicate that for both 4,6-DMDBT and tetralin conversion, Ni–Mo–S/Al_2O_3 is more affected by the N compound than Ni_2P/SiO_2. For Ni–Mo–S/Al_2O_3, the inhibition behavior of heterocyclic compounds is well documented [57,59,

Table 4
Catalytic activities of Ni_2P/SiO_2 and Ni–Mo–S/Al_2O_3 catalysts[a]

Catalyst	N content (%)	HDS conversion (%) (X_{A0})	HYD selectivity (%)	DDS selectivity (%)	TOF (10^{-5} s^{-1})	Specific rate (10^{-3} $\mu mol\ g^{-1}\ s^{-1}$)	Vol. rate ($mmol\ m^{-3}\ s^{-1}$)
Ni_2P/SiO_2	0	97	95	5	6.6	7.5	2.8
	0.02	85	94	6	5.8	6.6	2.4
Ni–Mo–S/Al_2O_3	0	60	70	30	4.1	11.8	7.2
	0.02	41	65	35	2.8	8.1	4.9

[a] $F_{A0} = 0.0163\ \mu mol\ s^{-1}$, TOF $= F_{A0}X_A/L$ (L, site loading, 240 μmol), specific rate $= F_{A0}X_A/W_{cat}$, Vol. rate $= F_{A0}X_A/V_{cat}$.

60]. The heterocyclic compounds are known to competitively adsorb on the active sites, particularly at lower temperatures (<613 K), where the adsorption is thermodynamically more favorable. It is thus understandable that competitive adsorption by the N compound on the Ni–Mo–S/Al_2O_3 catalyst leads to decreased conversion for both 4,6-DMDBT and tetralin. Catalytic activity was less affected by the N compounds in Ni_2P/SiO_2 than in Ni–Mo–S/Al_2O_3 catalyst, even though the HYD pathways were dominant for both 4,6-DMDBT and tetralin. It is also interesting to note that little change in the product selectivity in the HYD pathways occurred with decreasing conversion, indicating that hydrogenation and N-compound adsorption occur on different sites on the Ni_2P catalyst, likely the Ni centers and the P–OH groups, respectively.

Table 4 compares the performance of the Ni_2P/SiO_2 and Ni–Mo–S/Al_2O_3 catalysts based on turnover frequency (TOF), specific rate, and volumetric rate. The TOF tracks the conversion values (Fig. 11) as the rate measurements were made with equal sites loaded in the reactor. The TOF of the phosphide is higher than that of the sulfide by a factor of 1.6, which increases to 2.1 in the presence of N. For the specific and volumetric rates, the respective activity of the phosphide is smaller by factors of 1.6 and 2.6 in the absence of N and by factors of 1.2 and 2.0 in the presence of N. The lower specific and volumetric activities of the phosphide are likely due to the use of a low-density support (Cabosil) and the lack of optimization of the catalyst with respect to dispersion. Nonetheless, the high intrinsic rates as indicated by the TOFs suggest that the Ni_2P material is a promising material for further investigation.

4.4. *Bifunctional behavior of the Ni_2P/SiO_2*

The Ni_2P/SiO_2 catalyst shows unique acidic properties with a moderately strong intermediate between that of PO_x/SiO_2 (higher) and Ni–Mo–S/Al_2O_3 (lower), enabling protonation of pyridine and piperidine [47]. Moreover, the Ni_2P/SiO_2 catalyst shows a high hydrogenation behavior, probably due to its metallic nature. The FTIR studies of CO adsorption reveal that there are sufficient electrons on the Ni site to allow π-back bonding. It is known that π-back bonding is effective for molecular activation, as electrons fill antibonding orbitals. This enhances hydrogenation activity, as observed in metallic Ni, Pt, and Pd catalysts [61]. However, these metals are readily sulfided with loss of metallic character. A study of the electronic properties of SiO_2 supported Ni_2P, MoP, and MoS_2 catalysts using density functional calculations [62] has shown that the electron density around the metal followed the order $MoS_2/SiO_2 <$ MoP/$SiO_2 < Ni_2P/SiO_2$, which correlated well with the thiophene HDS activities of the catalysts. It was suggested that the higher electron density on the metal cation could enhance HDS activity by facilitating the dissociation of H_2 and the adsorption of thiophene [60,63]. The presence of P in Ni_2P prevents the compound from being bulk-sulfided and allows it to retain metallic properties for hydrogenation.

These results thus suggest that the supported Ni_2P catalyst has bifunctional properties, being able to carry out hydrogenation and protonation on metallic Ni and acidic PO–H sites, respectively. The catalytic bifunctional behavior is commonly found in highly dispersed noble metals supported on acidic materials like zeolites, which exhibit higher hydrogenation/dehydrogenation activity than those on nonacidic support [42,43]. But the noble metals are very sensitive to sulfur, which binds strongly with the metals and causes deactivation. The sulfur resistance of a bimetallic Pt–Pd catalyst has been shown to be due to a strong interaction between Pt and Pd [64]. In contrast to the noble metals, the supported Ni_2P catalysts exhibit high resistance to S and N compounds, particularly in hydrotreating [24,25,63]. A study of the effect of dispersion in Ni_2P catalysts supported on a high-surface area support (Si-MCM-41) showed that highly dispersed Ni_2P is particularly active for HDS and resistant to S and N compounds. It was suggested that a stronger interaction between Ni and P in the dispersed Ni_2P phase could enhance sulfur resistance [59]. Also, the resistance to N compounds is probably related to the acidic properties of the Ni_2P, which provides sites for the formation of the protonated N compounds as intermediate species in the HDN [47]. Thus these results imply that the remarkable activity of the supported Ni_2P catalyst has its origin in the proximity of the Ni and P species, which is responsible for the creation of proximal sites of high activity in hydrogenation and the activation of N and S compounds.

5. Conclusion

In this study, a nickel phosphide (Ni_2P) catalyst supported on a high-surface area SiO_2 (350 $m^2\ g^{-1}$) was prepared by a TPR method. The structural properties were characterized by powder XRD and EXAFS, which showed that the hexagonal Ni_2P phase was formed on the support and was stable during the reaction. The catalytic activities for HDS of 4,6-DMDBT and tetralin were tested on the Ni_2P/SiO_2 and Ni–Mo–S/Al_2O_3 catalyst samples at 573 K and 3.1 MPa. The results showed that without N compounds in the feed, the Ni_2P/SiO_2 catalyst exhibited much higher activities than the Ni–Mo–S/Al_2O_3 catalyst in HDS, with respective conversions of 97 and 60%. The addition of a quinoline led to a small decrease in HDS conversion (to 85%) for the Ni_2P/SiO_2 catalyst, but a large drop (to 41%) for the Ni–Mo–S/Al_2O_3 catalyst. Thus, the Ni_2P catalyst is tolerant of highly inhibitory N compounds. For Ni_2P/SiO_2, the HYD pathway in the desulfurization 4,6-DMDBT was dominant and was less inhibited by nitrogen compared with Ni–Mo–S/Al_2O_3. High hydrogenation activity was also obtained for the reaction of tetralin. The surface properties of the catalysts were examined by FTIR measurements of adsorbed CO and pyridine, which showed that the Ni_2P catalyst has a high electron density and is able to form π-back-bonded CO species on Ni sites, and that Ni_2P has moderate acidity in the form of PO–H sites that are able to protonate N compounds, such as pyridine and piperidine. These results thus suggest that the bifunctional properties of the supported Ni_2P catalyst probably contributed to the higher activity in hydrogenation and to high activity in the reaction of N and S compounds.

References

[1] K.A. Layman, M.E. Bussell, J. Phys. Chem. B 108 (2004) 10930.
[2] S.J. Sawhill, K.A. Layman, D.R. Van Wyk, M.H. Engelhard, C. Wang, M.E. Bussell, J. Catal. 231 (2005) 300.
[3] Energy Information Administration, Analysis: http://www.eia.doe.gov/oil_gas/petroleum/info_glance/crudeoil.html, December 2004.
[4] J.C. Schlatter, S.T. Oyama, J.E. Metcalfe, J.M. Lambert, Ind. Eng. Chem. Res. 27 (1988) 1648.
[5] H. Abe, T.K. Cheung, A.T. Bell, Catal. Lett. 21 (1993) 11.
[6] S.T. Oyama (Ed.), The Chemistry of Transition Metal Carbides and Nitrides, Blackie Academic and Professional, London, 1996.
[7] W.R.A.M. Robinson, J.N.M. van Gastel, T.I. Korányi, S. Eijsbouts, A.M. van der Kraan, J.A.R. van Veen, V.H.J. de Beer, J. Catal. 161 (1996) 539.
[8] T.I. Korányi, Appl. Catal. A 239 (2003) 253.
[9] W. Li, B. Dhandapani, S.T. Oyama, Chem. Lett. (1998) 207.
[10] C. Stinner, R. Prins, Th. Weber, J. Catal. 191 (2000) 438.
[11] C. Stinner, R. Prins, Th. Weber, J. Catal. 202 (2001) 187.
[12] P. Clark, W. Li, S.T. Oyama, J. Catal. 200 (2001) 140.
[13] S.T. Oyama, P. Clark, V.L.S. Teixiera da Silva, E.J. Lede, F.G. Requejo, J. Phys. Chem. B 105 (2001) 4961.
[14] C. Stinner, Z. Tang, M. Haouas, Th. Weber, R. Prins, J. Catal. 208 (2002) 456.
[15] S.T. Oyama, P. Clark, X. Wang, T. Shido, Y. Iwasawa, S. Hayashi, J.M. Ramallo-Lopez, F.G. Requejo, J. Phys. Chem. B 106 (2002) 1913.
[16] D.C. Phillips, S.J. Sawhill, R. Self, M.E. Bussell, J. Catal. 207 (2002) 266.
[17] S.T. Oyama, J. Catal. 216 (2003) 343.
[18] N.P. Sweeny, C.S. Rohrer, O.W. Brown, J. Am. Chem. Soc. 80 (1958) 799.
[19] E.L. Muetterties, J.C. Sauer, J. Am. Chem. Soc. 96 (1974) 3410.
[20] F. Nozaki, R. Adachi, J. Catal. 40 (1975) 166.
[21] F. Nozaki, M. Tokumi, J. Catal. 79 (1983) 207.
[22] P. Clark, S.T. Oyama, J. Catal. 218 (2003) 78.
[23] P. Clark, X. Wang, S.T. Oyama, J. Catal. 207 (2002) 256.
[24] S.T. Oyama, X. Wang, Y.-K. Lee, K. Bando, F.G. Requejo, J. Catal. 210 (2002) 207.
[25] A. Wang, L. Ruan, Y. Teng, X. Li, M. Lu, J. Reng, Y. Wang, Y. Hu, J. Catal. 229 (2005) 314.
[26] S.J. Sawhill, D.C. Phillips, M.E. Bussell, J. Catal. 215 (2003) 208.
[27] S.T. Oyama, X. Wang, Y.-K. Lee, W.-J. Chun, J. Catal. 221 (2004) 263.
[28] A. Marafi, S. Fukase, M. Al-Marri, A. Stanislaus, Energy Fuels 17 (2003) 661.
[29] A.L. Ankudinov, B. Ravel, J.J. Rehr, S.D. Congradson, Phys. Rev. B 58 (1998) 7565.
[30] S. Rundqvist, Acta Chem. Scand. 16 (1962) 992.
[31] D.E.C. Corbridge, Studies in Inorganic Chemistry, vol. 10, fourth ed., Elsevier, Amsterdam, 1990.
[32] E.A. Stern, Phys. Rev. B 48 (1993) 9825.
[33] D.C. Koningsberger, R. Prins (Eds.), X-Ray Absorption: Principles and Techniques of EXAFS, SEXAFS and XANES, Wiley, New York, 1989.
[34] Z. Liu, M. Meng, Y. Fu, M. Jiang, T. Hu, Y. Xie, T. Liu, Mater. Lett. 54 (2002) 364.
[35] K.I. Hadjiivanov, G.N. Vayssilov, Adv. Catal. 47 (2002) 307.
[36] E.E. Platero, D. Scarano, G. Spoto, A. Zecchina, Faraday Discuss., Chem. Soc. 80 (1985) 183.
[37] J.B. Peri, J. Catal. 86 (1984) 84.
[38] J.B. Peri, Discuss. Faraday Soc. 41 (1966) 121.
[39] B. Müller, A.D. van Langeveld, J.A. Moulijn, H. Knözinger, J. Phys. Chem. 97 (1993) 9028.
[40] M. Angulo, F. Maugé, J.C. Duchet, J.C. Lavalley, Bull. Soc. Chim. Belg. 96 (1987) 925.
[41] B.M. Vogelaar, P. Steiner, A.D. van Langeveld, S. Eijsbouts, J.A. Moulijn, Appl. Catal. A 251 (2003) 85.
[42] B.M. Vogelaar, P. Steiner, A.D. van Langeveld, S. Eijsbouts, J.A. Moulijn, Appl. Catal. A 251 (2003) 85.
[43] L. Hu, G. Xia, L. Qu, M. Li, C. Li, Q. Xin, D. Li, J. Catal. 202 (2001) 220.
[44] B.H. Cooper, B.B.L. Donnis, Appl. Catal. A 137 (1996) 203.
[45] M.R. Basila, T.R. Kantner, K.H. Rhee, J. Phys. Chem. 68 (1964) 3197.
[46] A.P. Legrand, H. Hommel, A. Tuel, Adv. Colloid Interface Sci. 33 (1990) 91.
[47] J. Ward, in: J.A. Rabo (Ed.), Zeolite Chemistry and Catalysis, in: ACS Monograph, vol. 171, Am. Chem. Soc., Washington, DC, 1976.
[48] S.T. Oyama, Y.-K. Lee, J. Phys. Chem. 109 (2005) 2109.
[49] D.R. Kilanowski, T. Teeuwen, V.H.J. de Beer, B.C. Gates, G.C.A. Schuit, H. Kwart, J. Catal. 55 (1978) 129.
[50] T. Kabe, A. Ishihara, H. Tajima, Ind. Eng. Chem. Res. 31 (1992) 1577.
[51] B.C. Gates, H. Topsøe, Polyhedron 16 (1997) 3213.
[52] M. Houalla, D.H. Broderick, A.V. Sapre, N.K. Nag, V.H.J. de Beer, B.C. Gates, H. Kwart, J. Catal. 21 (1980) 523.
[53] X. Ma, K. Sakanishi, I. Mochida, Ind. Eng. Chem. Res. 33 (1994) 218.
[54] D.D. Whitehurst, T. Isoda, I. Mochida, Adv. Catal. 42 (1998) 345.
[55] K. Segawa, S. Satoh, Stud. Surf. Sci. Catal. 127 (1999) 129.
[56] M. Egorova, R. Prins, J. Catal. 224 (2004) 278.
[57] J.H. Kim, X. Ma, C. Song, Y.-K. Lee, S.T. Oyama, Energy Fuels 19 (2005) 353.
[58] K.G. Knudsen, B.H. Cooper, H. Topsøe, Appl. Catal. A: Gen. 189 (1999) 205.
[59] Y. Shu, Y.-K. Lee, S.T. Oyama, J. Catal. 236 (2005) 112.
[60] H. Topsøe, B.S. Clausen, F.E. Massoth, in: J.R. Anderson, M. Boudard (Eds.), Catalysis Science and Technology, vol. 11, Springer-Verlag, New York, 1996.
[61] J.E. Huheey, E.A. Keiter, R.L. Keiter, Inorganic Chemistry: Principles of Structure and Reactivity, fourth ed., Harper Collins College Publishers, New York, 1993.
[62] J.A. Rodriguez, J.-Y. Kim, J.C. Hanson, S.J. Sawhill, M.E. Bussell, J. Phys. Chem. B 107 (2003) 6276.
[63] J.A. Rodriguez, J. Phys. Chem. B 101 (1997) 7524.
[64] R.M. Navarro, B. Pawelec, J.M. Trejo, R. Mariscal, J.L.G. Fierro, J. Catal. 189 (2000) 184.